

Smart navigation through a rotating barrier: Deep reinforcement learning with application to size-based separation of active microagents

Mohammad Hossein Masoudi^{1,*} and Ali Naji^{2,1,†}

¹*School of Nano Science, Institute for Research in Fundamental Sciences (IPM), Tehran 19538-33511, Iran*

²*Department of Physics, College of Science, Sultan Qaboos University, Muscat 123, Oman*

We employ deep reinforcement learning methods to investigate shortest-time navigation strategies for smart active Brownian particles (agents) that self-propel through a rotating, localized potential barrier in an otherwise static and viscous fluid background. The particle motion is prescribed to begin from a specified start point and terminate at a specified destination point. The potential barrier is modeled as a repulsive Gaussian potential with a finite range that rotates with given angular velocities around a fixed center within the plane of motion. We use an advantage actor-critic approach to train the agents and demonstrate that, by leveraging this approach, the rotating potential can be utilized for size-based sorting and separation of the agents. In other words, agents of different (hydrodynamic) radii reach the end-point at sufficiently well-separated times, enabling their separation. The efficiency of particle separation in this context is discussed using specific criteria. We also study the effect of rotational Brownian noise on the quality of the proposed size-based sorting mechanism. Additionally, we demonstrate how the use of noise-induced training can enhance this mechanism in a noisy background within the range of parameters explored in our work. Reinforcement learning in the context of active particles thus offers promising avenues to unravel optimal navigation strategies within complex environments, with potential applications that can be utilized in microfluidic settings.

I. INTRODUCTION

Active matter refers to a broad class of soft materials that involve active particles capable of converting ambient free energy available into self-propulsive motion in a viscous background (such as aqueous media) [1]. Examples of active particles include molecular motors within the cell, microorganisms such as bacteria, and synthetic colloids such as Janus particles [2–4]. These microagents display nearly ballistic self-propulsion over a characteristic run time which is followed (or accompanied) by stochastic reorientation events. Systems of active particles exhibit a rich phenomenology due to their inherent nonequilibrium dynamics that exacerbate other factors (such as noncentral interparticle alignment effects, long-range hydrodynamic interactions, strong particle coupling to confining boundaries, etc), which contribute to their complex collective properties [5–19].

The mechanisms of self-propulsion in active agents can vary widely. Biological microorganisms propel by modulating various modes of motion in their cellular organelles such as flagella and cilia [11, 20, 21]. Synthetic active colloids [4, 10, 22–25], on the other hand, utilize catalytic surface activity to produce self-propulsive force, driving their autonomous locomotion in fluid media. In most cases, the pattern of motion may vary also in response to surrounding stimuli and external fields such as chemical nutrient fields (as in chemotactic bacteria [26]), light intensity (as in phototactic active particles [27]), Earth’s gravitational field (as in gyrotactic algae [28]), and exter-

nal magnetic fields (as in magnetotactic bacteria [29, 30] and active dipolar spheroids [31]).

Despite the diversity of its examples, the generic aspects of self-propelled motion in active microagents can be captured within minimal models [32] such as the so-called model of active Brownian particles (ABPs). In the most basic formulation of this model, the self-propulsion speed of ABPs is assumed to be constant and the reorientation mechanism is provided by the ambient rotational Brownian (thermal) noise. The simplicity of this and other similar models has enabled their integration with reinforcement learning (RL) methods to study optimal navigation (or other task performances) by self-propelled agents in an otherwise complex environment [33–43] where the plane of motion is stationary. Recent works in this context include path planning of ABPs [33] using RL to discover the optimal shortest-time paths through a static Mexican hat potential [33] between two specified start and end points, and planning optimal escape strategies for gyrotactic particles trapped in the Green-Vortex flow [34]. RL methods have also been utilized for active navigation through a nonstationary plane of motion such as an unsteady chaotic [35] or turbulent flow [39, 44]. On the other hand, advancement of deep reinforcement learning (DRL) techniques in obtaining nonlinear optimal policy functions through neural networks have proven advantageous in exploiting enhanced optimal strategies for active navigation through unsteady vortical flows [45] or in complex (but steady) environments such as a shear flow through a pipe or a Gaussian random potential [37].

Despite the aforementioned advances in studying smart navigation through global time-varying flows [39, 45], navigation strategies through localized, time-varying perturbations such as a moving barrier in the surround-

* mh.masoudi@ipm.ir

† a.naji@ipm.ir

ing medium remain unexplored. An example of the latter case, which will be the focus of the present work, would be a repulsive potential with a finite support (or range of action), moving in a periodic fashion within an otherwise static environment being navigated by an active agent. The regular pattern of motion in the environment is expected to enhance the controllability of the shortest-time navigation process based on agent-specific parameters, paving the way for possible particle-based applications in microscale settings. In this work, we investigate such a case by introducing a model of smart active Brownian particles (sABPs) in which the self-propelled agent is equipped by a DRL algorithm, based on the advantage actor-critic (A2C) method, which enables its optimal, shortest-time navigation through a rotating Gaussian potential barrier. We demonstrate that such a design can indeed be used to sort and separate microparticles based on their size, a process which is of major relevant to microfluidic applications [46–48]

We also investigate how the rotational Brownian noise can be integrated into agent-training procedures via the provided DRL algorithm and, hence, show how the presence of noise affects the predicted size-based sorting of the agents within our model. Interestingly, however, we find that noise-induced training can improve the precision of our size-based sorting compared to the noise-free case and the cases where agents are trained with lower intensity of noises.

The paper is organized as follows: Our model and methods are discussed in Secs. II and III. The results on optimal trajectories appear in Sec. IV. We also discuss the details and potential applications of our proposed DRL algorithm in the next parts of Sec. IV, and demonstrate in Sec. IV C how the noise-induced training can impact such applications.

II. MODEL

We use a two-dimensional (2D) smart navigation model comprising three main components: (i) an agent modeled as a colloidal particle that, in the absence of learning strategies, exhibits a self-propelled motion subject to ambient noises in an assumed viscous fluid; (ii) an inhomogeneous environment where the microagent faces a finite-range, dynamically evolving potential barrier, as it moves from a prescribed start point S to a given destination point (or goal) G in the $x - y$ plane (see Fig. 1); and (iii) a DRL framework that trains the model microagent to achieve shortest-time navigation through the said environment. According to (i), the model microagent behaves as a minimal active Brownian particle (ABP) [32] at its baseline. Hence, by analogy, we refer to it as a smart active Brownian particle (sABP) when it is equipped with component (iii). Further specifics of the aforesaid components are discussed in what follows.

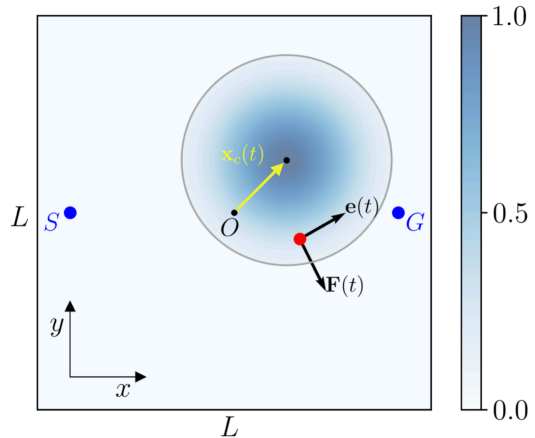


Figure 1. Schematic view of a microagent navigating shortest-time trajectories from S to G on a 2D plane where it encounters a rotating, repulsive Gaussian potential (color-coded disklike region). The instantaneous position vector of the center of the potential from the origin, O , is denoted by $\mathbf{x}_c(t)$ and the range of the potential is demonstrated by the dark gray circle. While equipped with a DRL algorithm, the microagent self-propels along the instantaneous orientation unit vector $\mathbf{e}(t)$ against a rotational ambient noise and a force $\mathbf{F}(t)$ from the rotating potential. The system is confined inside a square box of side length L . The colorbar on the right indicates the rescaled strength of the potential U/U_0 (see the text).

A. Equations of motion without learning

The agent is assumed to be a spherical particle of radius a_p whose position and orientation coordinates are confined to a 2D square box of side length L , with the origin $(0, 0)$ chosen at its center; see Fig. 1. In the absence of learning, evolve according to the active, overdamped Langevin equations [32] (modeling component i)

$$\dot{\mathbf{x}}(t) = v_0 \mathbf{e}(t) + \gamma_T^{-1} \mathbf{F}(\mathbf{x}(t), t), \quad (1)$$

$$\dot{\theta}(t) = -\alpha \Omega(\mathbf{x}(t), \theta(t), t) + \xi_R(t). \quad (2)$$

Here, $\mathbf{x}(t) = (x(t), y(t))$ denotes the position coordinates of the microagent and v_0 is its constant self-propulsion speed, pointing along the unit vector $\mathbf{e}(t) = (\cos \theta(t), \sin \theta(t))$ that makes an angle $\theta(t)$ relative to the x -axis; see Fig. 1.

In Eq. 1, γ_T is the translational friction coefficient, while $\mathbf{F}(\mathbf{x}(t), t) = -\nabla U(\mathbf{x}(t), t)$ (which we may indicate by $\mathbf{F}(t)$ for simplicity) is the deterministic force that stems from the interaction of microagent with a repulsive potential barrier $U(\mathbf{x}(t), t)$ that it encounters on its way from S to G in the surrounding environment (modeling component ii). The potential barrier is assumed to be a rotating Gaussian centered at $\mathbf{x}_c(t)$, with standard deviation σ and a radius of influence R_c (cutoff), limiting the range of its action (Fig. 1):

$$U(\mathbf{x}(t), t) = U_0 e^{-|\mathbf{x}(t) - \mathbf{x}_c(t)|^2 / 2\sigma^2} \quad (3)$$

when $|\mathbf{x}(t) - \mathbf{x}_c(t)| \leq \sigma$, and $U(\mathbf{x}(t), t) = 0$ otherwise. For simplicity, we take $R_c = |\mathbf{x}_c(t)|$. The locus of the Gaussian peak rotates at constant angular speed ω ; hence, $\mathbf{x}_c(t) = R_c(\cos \omega t, \sin \omega t)$.

In Eq. 2, $\xi_R(t)$ is the rotational Brownian noise with zero mean and two-point correlator $\langle \xi_R(t)\xi_R(t') \rangle = 2D_R\delta(t-t')$, where D_R is the rotational diffusivity that relates to the rotational friction coefficient γ_R through the Smoluchowski-Einstein relation $D_R = k_B T / \gamma_R$, with T being the temperature and k_B is the Boltzmann constant (note that the translational noise is of no significance at sufficiently high Péclet numbers that are of interest here and is thus ignored in Eq. 1. see e.g., Refs. [33, 43]). For concreteness, we assume that the translational and rotational friction coefficients are of Stokes forms $\gamma_T = 6\pi\eta a_p$ and $\gamma_R = 8\pi\eta a_p^3$, respectively.

Our modeling component (iii) enters through the term $-\alpha\Omega(\mathbf{x}(t), \theta(t), t)$ in Eq. 2. However, before proceeding to discuss this further (Section II B), we note that, in the context of nonsmart ABPs, such a term represents a deterministic angular velocity that can originate from an intrinsic particle chirality or an external stimuli/fields (e.g., due to magnetic/gyrotactic torques experienced by dipolar active particles in external magnetic/gravitational fields or even klinotactic reorientation rates that certain types of active particles can exhibit in response to chemotactic fields; see Ref. [31] and the original reference cited therein).

B. Equations of motion with DRL

Within the DRL framework, the sABP predicts its preferred orientation $\mathbf{e}_{\text{pref}}(t) = (\cos \theta_{\text{pref}}(t), \sin \theta_{\text{pref}}(t))$ at any moment in time by requesting the A2C network to steer it toward the destination optimally. Here, $\theta_{\text{pref}}(t)$ denotes the corresponding predicted preferred orientation angle relative to the x -axis. With further details provided in Sec. III A, here we only note how the DRL is incorporated in the equations of motion.

In case of rotational thermal noises, the angular fluctuations, by defining $\psi(t) = \theta(t) - \theta_{\text{pref}}(t)$ and characterizing the reorienting mechanism by $\Omega(\mathbf{x}(t), \theta(t), t) = \psi(t)$ similar to Ref. [33], we arrive at the following Langevin equation to determine the time evolution of angular fluctuations:

$$\dot{\psi}(t) = -\alpha\psi(t) + \xi_R(t), \quad (4)$$

While this equation is similar to the one used in Ref. [33], our approach involves certain methodological differences relative to the said reference. To highlight these differences, we need to outline two conceptual stages: the ‘training stage’ and the ‘simulation stage’ in the numerical implementation of the DRL approach. During the training stage, the agent continually strives to find better policies, which, in our case, means finding shorter trajectories until reaching the optimal policy equivalent to predicting steering angles $\theta_{\text{pref}}(t) \simeq \theta_{\text{opt}}(t)$, and in the

simulation stage, we can test the shortest-time trajectories of the agent by following the optimal policy obtained from the converged A2C network at the end of the training stage.

When considering the main differences, it’s important to note that in Ref. [33], the agent can only be simulated in a noisy background environment. During the training stage, when $\theta_{\text{opt}}(t)$ is obtained through the Q-learning algorithm, the thermal noises are not applied. They can only be analyzed during the simulation stage. On the other hand, our approach allows the agent to be trained and tested in noisy backgrounds during both the training and simulation stages.

Secondly, the tabular Q-learning algorithm used in Ref. [33] is best suited for discretized background environments, typically involving a lattice-presumed plane of motion where the space is divided into a finite grid of cells. In contrast, our approach allows for continuous prediction of the shortest-time trajectory, providing a more flexible and accurate solution for dynamic environments.

C. Dimensionless representation

To avoid redundancies in the number of parameters and simplify the equations of motion, we introduce dimensionless quantities by non-dimensionalizing the scales of length with a reference sABP diameter d as $x \rightarrow x/d$ and $y \rightarrow y/d$. Other quantities are rescaled as $t \rightarrow tv_0/d$, $U \rightarrow U/U_0$, $\mathbf{F} \rightarrow \mathbf{F}/F_0$ where we have defined $F_0 = U_0/d$, $\gamma_T \rightarrow \gamma_T v_0 d / U_0$, $\gamma_R \rightarrow \gamma_R v_0 / (U_0 d)$ and $D_R \rightarrow D_R d / v_0$. The rescaled rotational diffusivity is nothing but the inverse Péclet number defined as

$$\text{Pe} = v_0 / (D_R d). \quad (5)$$

Equation 2 is then written in non-dimensional form for components $x(t)$ and $y(t)$ as

$$\frac{dx(t)}{dt} = \cos \theta(t) - \gamma_T^{-1} \frac{\partial U(x, y, t)}{\partial x}, \quad (6)$$

$$\frac{dy(t)}{dt} = \sin \theta(t) - \gamma_T^{-1} \frac{\partial U(x, y, t)}{\partial y}. \quad (7)$$

Equation 4 on the other hand, remains in the exact same form by rescaling $\alpha \rightarrow \alpha d / v_0$. The correlator of the rescaled noise $\xi_R \rightarrow \xi_R d / v_0$ then follows as $\langle \xi_R(t)\xi_R(t') \rangle = 2\text{Pe}^{-1}\delta(t-t')$ in rescaled units.

III. METHODS

A. Utilizing DRL for navigating sABP

In our implementation, the sABP interacts with its surrounding environment by perceiving (or, observing) the physical position as its *state* at time t , $s_t =$

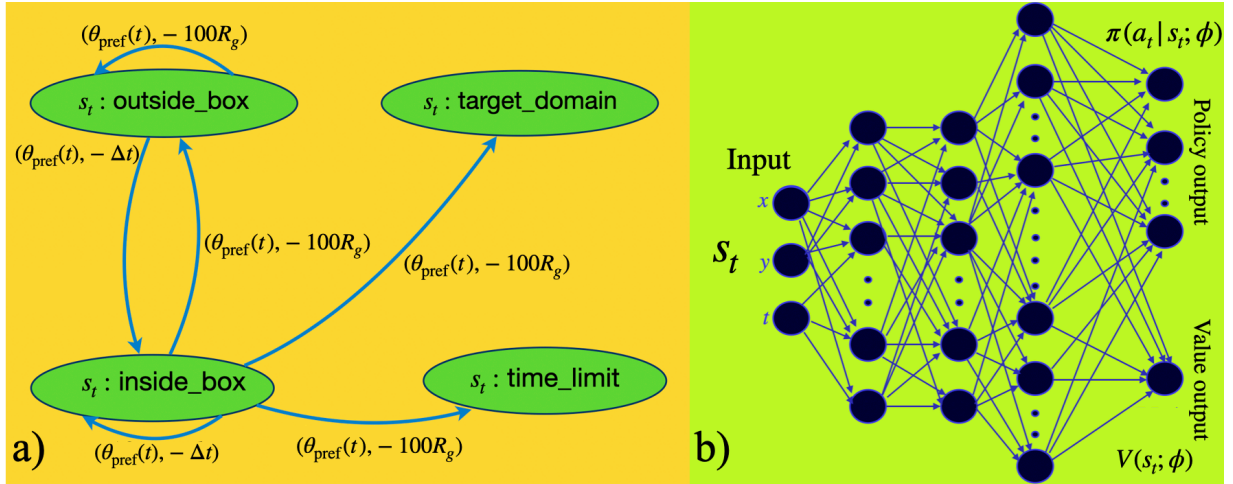


Figure 2. Panel (a): MDP diagram for optimal navigation in the shortest time. Each edge demonstrates a pair of actions and rewards (a_t, r_t) obtained by transitioning from state s_t to a new state $s_{t+\Delta t}$. Also, four classes of states are represented by different labels: “inside_box”, “outside_box”, “time_limit” and “target_domain”. Panel (b): A2C network diagram with input layer s_t , body and output layers as represented by the policy $\pi(a_t|s_t)$ and value $V(s_t)$ output functions.

$(x(t), y(t))$. Each state s_t belongs to the space \mathcal{S} of all possible positional states within the simulation box. When perceiving the state s_t at time t , the sABP selects action a_t by picking a steering angle $\theta_{\text{pref}}(t)$ from all possible angles $\mathcal{A} = \{m\pi/l | m = 0, 1, 2, \dots, l\}$ at angular separation π/l , where $l > 0$ is a given angular resolution parameter that allows for fine-tuning between coarse and precise navigation controls.

To implement the aforesaid action, we update the direction of self-propulsion at the beginning of each prediction time step (Δt) as follows: $\mathbf{e}(t) \leftarrow \mathbf{e}_{\text{pref}}(t)$, where $\mathbf{e}_{\text{pref}}(t) = (\cos \theta_{\text{pref}}(t), \sin \theta_{\text{pref}}(t))$. This process involves integrating the translational and rotational equations of motion in Eqs. 1 and 2 to determine the new state of the sABP in the next state $s_{t+\Delta t}$. To achieve this, numerical integration of equations of motion is carried out through simulation time steps (δt) for the translational and rotational dynamics of the agent, distinct from the prediction time step (Δt) . Throughout the integration process within the prediction time step, we track the exerted force $\mathbf{F}(t)$ in much shorter time steps $(\delta t \ll \Delta t)$

until reaching the next state of the agent at $t + \Delta t$. The agent then receives a *reward* signal, r_t , from the environment at the end of Δt , as illustrated in Fig. 2(a).

The preceding decision-making process (performed by selecting the desired actions) is modelled as a Markov Decision Process (MDP) [49], a mathematical framework that provides a formalization for stochastic sequential decision-making problems. This is shown schematically in panel (a) of Fig. 2 where the states are depicted as closed ellipses and the pairs of action and reward (a_t, r_t) by interconnecting directed arrows. The provided MDP diagram has two classes of states: non-terminal and terminal. The non-terminal states are labelled “inside_box” and “outside_box”, indicating that the agent has not yet reached a terminal state. Conversely, the terminal states are labeled “time_limit” and “target_domain”. The “time_limit” state represents the scenario where the agent fails to reach the target domain within the specified time limit T_{max} . The “target_domain” state indicates that the agent has successfully reached the target domain at the destination point G (see Fig. 1) in less

time than T_{\max} . Through this MDP process, we have the following rewarding system: Movements are determined by selecting actions a_t at each time step within the simulation box, resulting in a penalty for our agent of $r_t = -\Delta t$, where Δt represents the time step required for the agent to translocate between two consecutive states. In case of being in states labelled by “outside_box”, and “time_limit”, we penalized the agent by $r_t = -100R_g$ where R_g is defined as the in-plane distance between the terminal state outside the target domain and the destination point (this penalty adjustment are especially useful to avoid local optima and reach more rapidly to the shortest path). In this MDP diagram, transitioning to the target domain is awarded by a huge positive value of +100 that helps the sABP discover the target domain. By formulating our problem within an MDP and utilizing DRL as we discuss next, We predict the approximate optimal *policy* function using a DRL approach that can guide the agent to reach the target domain in the shortest possible time. In this section, we closely follow the methodology explained in Refs. [37, 38, 50]. We refer the reader to these refs for further details.

B. Incorporating the A2C method

We implement the A2C method, merging the strengths of value-based and policy-based RL approaches. We closely pursue the details of the A2C method in Ref. [51] and implement the method with the PyTorch [52] library. The A2C method is structured around two key components: the actor-network, denoted as $\pi(a_t|s_t; \phi)$, and the critic network, represented by $V(s_t; \phi)$. Both the actor and critic networks are parameterized by a shared set of parameters ϕ , facilitating a unified approach to obtain the optimal policy and value function. The essence of the A2C model lies in its advantage function, $A(a_t, s_t; \phi) = Q(a_t, s_t) - V(s_t; \phi)$, which evaluates the relative benefit of taking action a_t in state s_t denoted by the action-value function $Q(a_t, s_t)$ under the policy $\pi(a_t|s_t; \phi)$ compared to the baseline value provided by the critic network as the value function $V(s_t; \phi)$. Here, the action-value function can be approximated through $Q(a_t, s_t) \simeq G_t$ where the cumulative discounted rewards are defined as $G_t = \sum_{t'=t}^{T_{\max}} \gamma^{t'} r_{t'}$, where T_{\max} corresponds to the time required for the agent to reach the terminal state and γ determines the discounting factor.

The critic-network aims to minimize the squared advantage, formulated as $L_V(\phi) = \chi A^2(a_t, s_t; \phi)$, where χ is a coefficient that balances the emphasis on the value function loss. In parallel, the actor-network strives for policy optimization by minimizing its loss, $L_\pi(\phi) = -\beta \ln \pi(a_t|s_t; \phi) \cdot A(a_t, s_t; \phi) - \xi H(\pi(a_t|s_t; \phi))$, and the β coefficient weigh the effect of policy losses. We also employ the entropy term, $H(\phi) = -\sum_{a_t} \pi(a_t|s_t; \phi) \ln \pi(a_t|s_t; \phi)$ weighted by ξ , to encourage exploration and prevent the premature convergence to suboptimal policies. Both networks concur-

rently adjust their shared parameters ϕ through gradient descent: $\phi \leftarrow \phi + \nabla_\phi L_V(\phi)$ and $\phi \leftarrow \phi + \nabla_\phi L_\pi(\phi)$.

The architecture of our A2C network is structured with three principal layers: an input layer that processes the spatial and temporal variables x , y , and t ; a processing layer composed of two sub-layers, and an output layer with two separate policy and value function outputs. The policy output is tasked with generating stochastic policies, $\pi(a_t|s_t; \phi)$, which calculates the probability of selecting each action a_t from the set of possible actions. This involves choosing the steering angle from a set of discrete angles at the beginning of each time step. Simultaneously, the value output, $V(s_t; \phi)$, estimates the expected returns from state s_t , essential in computing the advantage function and guiding the policy towards more rewarding actions.

C. Training sABP by employing A2C method

In training our agents via the A2C method, we continually attempt to obtain the optimal policy in sequential episodes. Each episode in the context of RL starts at the initial state (in the case of our navigation problem, corresponds to the starting point located at S as denoted in Fig. 1) and ends when the termination criteria, as clearly explained in Sec. III A, are met. The first episode is initially started with our A2C network randomly weighted. Through each episode of learning, based on the predictions obtained by our A2C network, we will be able to generate the fixed number of trajectories (N) following the policy $\pi(a_t|s_t; \phi)$ (as aforementioned, our A2C network are parameterized by ϕ , determining the current weights of A2C network). The sABP generates trajectories τ_ϕ , which are time-sequential sets of states and actions ($s_0, a_0, s_1, a_1, \dots, s_T$), starting from initial state s_0 and terminating in final state s_T aimed at maximizing the cumulative rewards.

During the training phase, the agent generates trajectories with fixed time intervals, Δt , under the guidance of a trainable stochastic policy, $\pi(a_t|s_t; \phi)$. The losses computed for both the policy function, $L_\pi(\phi)$, and the value function, $L_V(\phi)$, are collectively averaged across these trajectories. These aggregated loss values are then utilized for back-propagation to update the weights of the interconnected A2C network. The training objective is to minimize the total loss, $L(\phi) = L_V(\phi) + L_\pi(\phi)$.

D. Choice of parameters for training agents

In our specific problem, we train sABP using the A2C network as described in Sec. III B. The agent, with a radius $a_p = 1$ (significantly smaller than the simulation box length L), starts at coordinates $(x, y) = (-25, 0)$. For the potential barrier we have $|\mathbf{x}_c(t)| = 10$ and a cutoff radius $R_c = 10$ as for the simplicity we take $R_c = |\mathbf{x}_c(t)|$. The target domain is a circular region centred around

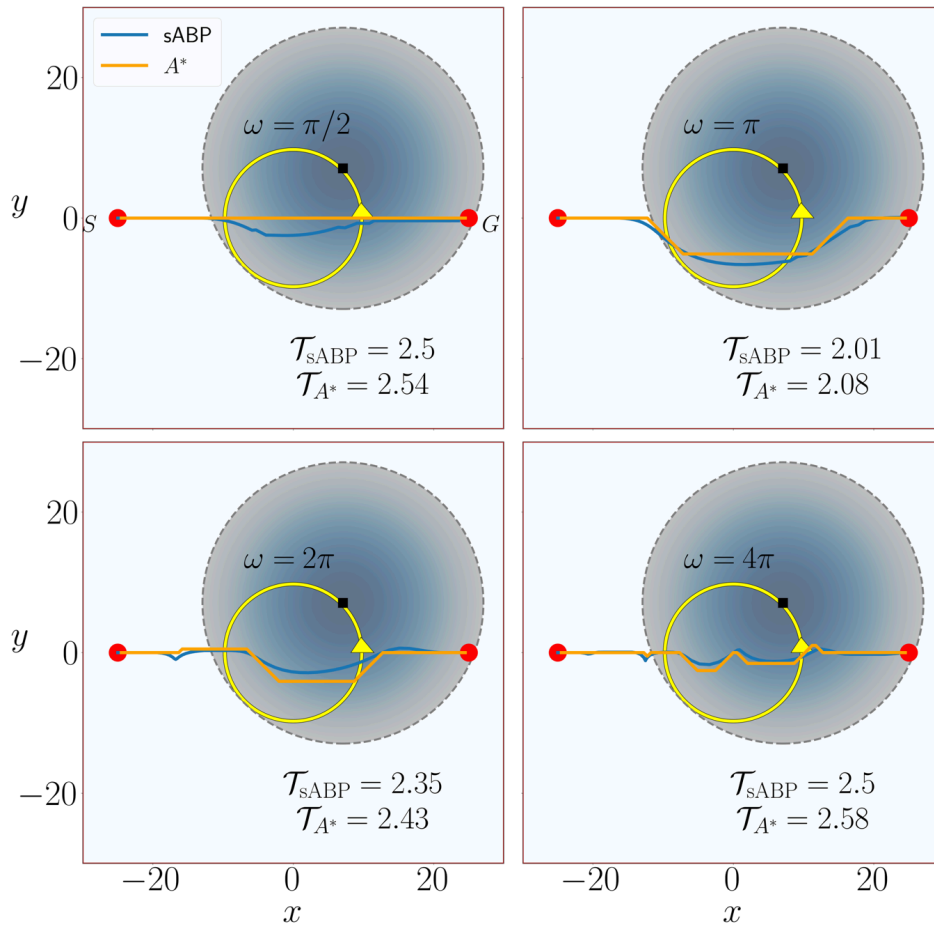


Figure 3. Shortest-time S-to-G trajectories of the modelled sAPB through a repulsive Gaussian potential whose center rotates in counterclockwise direction along the yellow circle with angular velocities $\omega = \{\pi/2, \pi, 2\pi, 4\pi\}$ (as appeared by the snapshots of the dark blue region at $t = \{1/2, 1/4, 1/8, 1/16\}$), as shown on the graphs. Blue trajectories represent the sABP trajectory obtained via the present DRL algorithm, and orange trajectories show the shortest-time trajectory implemented by the A^* algorithm.

$(x, y) = (25, 0)$ with a radius of 0.5, which is equal to half of the referenced diameter of the ABP. And also the time limit is set by $T_{\max} = 20$.

We perform the training with a constraint where the equality $F_{\max} = v_0/\gamma_T$ holds. Given the Gaussian potential amplitude $U_0 = k_B T$, we derive $\gamma_T = U_0/(2\sigma v_0)$. Furthermore, some straightforward calculations result in a viscosity $\eta \simeq 0.001$ Pa·s, which agrees with that of water at room temperature, confirming the feasibility of our model for synthetic microagents operating in aqueous environments.

We train sABP over 20,000 episodes in our implementation, averaging 10 trajectories per episode. We tune hyper-parameters of A2C network (appeared in panel (b) of Fig. 2) by setting $\chi = 10^{-4}$, $\beta = 10^{-3}$, $\xi = 0.5$ and $\gamma = 0.99$. At each prediction time step $\Delta t = 5 \times 10^{-2}$ (see Sec. III A), the A2C network determines direction of $\mathbf{e}_{\text{pref}}(t)$ among $l = 64$ steering angles. We also set $\delta t = \Delta t/50$ in our implementation.

IV. RESULTS AND DISCUSSIONS

In this section, we obtain the shortest-time trajectories, corresponding to four specific rotational velocities $\omega = \{\pi/2, \pi, 2\pi, 4\pi\}$. To ensure the consistency of our results in obtaining optimal policies, we conduct multiple training sessions, each of them starting from an initial episode and terminating at a final episode. This will allow us to verify that the optimal policies are uniquely achieved across different training sessions. Additionally, we validate the optimality of our results demonstrated as blue trajectories in Fig. 3 by comparing them with those we obtain from a graph-based algorithm A^* , shown as orange trajectories in Fig. 3. It is implemented based on the algorithm provided in Ref. [53] for finding the shortest-time trajectory in the dynamical background, which we adapt here for the case of ABPs.

By far, we have focused on utilizing the A2C deep reinforcement learning method to achieve the objective of

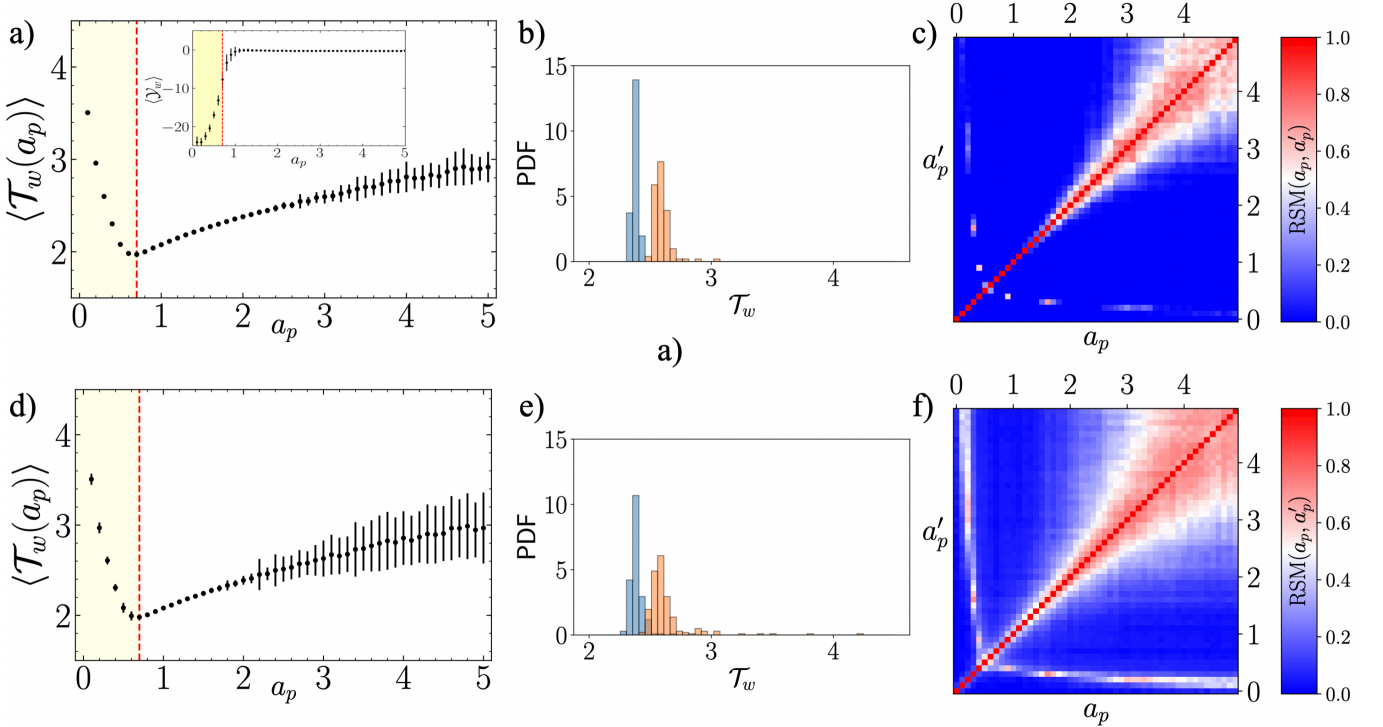


Figure 4. Panel (a): the wall arrival time \mathcal{T}_w versus different size of sABPs in noise-free scenario where $\text{Pe}^{\text{sim}} = \infty$. The inset shows \mathcal{Y}_w versus all simulation sizes. Panel (b) shows the overlapped histogram of wall arrival times $\mathcal{T}_w(a_p = 2.0)$ and $\mathcal{T}_w(a_p = 3.0)$. In panel (c), we demonstrate $\text{RSM}(a_p, a'_p)$ of sABPs of sizes a_p and a'_p . Panels (d), (e) and (f) are the same as panels (a), (b) and (c), respectively, but they represent the results for a noisy background with $\text{Pe}^{\text{sim}} = 10^2$.

navigating a time-varying background potential and enabling sABP to reach the destination in the shortest possible time.

Moving forward, we will explore additional applications that can be derived from our A2C learning method. These applications are discovered by simulating sABP of various sizes and investigating their behaviour within different background environments, including settings such as different Péclet numbers and sizes utilized during the training episodes. By examining these scenarios, we can further assess the applications of our A2C method in diverse settings.

A. Size-based particle sorting mechanism for the sABP

This section will explore simulations employing the A2C method to navigate sABPs to reach the wall area (extending across both sides of the target domain along the y -axis with the same x). Our primary objective is to sort and separate the sABPs based on their wall arrival times rather than directly measuring their physical sizes.

To accomplish this objective, in the simulation stage, we assume the size of the sABPs in the range of discrete intervals of $a_p \in \mathcal{A}_p = \{0.1, 0.2, \dots, 5\}$, where we derive the control parameters $\mathbf{e}_{\text{pref}}(t)$ according to the A2C network trained for optimal navigation of unit size ($a_p = 1$) micro-agent. Subsequently, we plot the arrival times at the designated wall area versus the full range of sizes \mathcal{A}_p of the sABPs as displayed in panel (a) of

Fig. 4. Therefore, we realize an exciting, unique map between the average of wall arrival times ($\langle \mathcal{T}_w \rangle$) and their respective sizes a_p (with this important outcome that approximately all the micro-agents with $a_p \geq 1$ reach to the target domain with $\langle \mathcal{Y}_w \rangle \simeq 0$ as appeared in the inset of panel (a) in Fig. 4). It is noticeable that there are two distinct trends of mean wall arrival times; one descending for $a_p < a_p^*$ and the other ascending for $a_p > a_p^*$, where a_p^* is the size that we refer to as the minimum arrival time of sABPs. By analyzing these two size ranges separately, we can accurately determine the size of each particle based on the corresponding mean wall arrival time. On the other hand, if we consider the whole range of sizes \mathcal{A}_p , we can not precisely separate particles according to their sizes. It mainly happens because each pair of distinct sABPs with sizes a_p, a'_p ($a_p \neq a'_p$), $a_p < a_p^*$ and $a'_p > a_p^*$ would hit the wall area on average simultaneously $\langle \mathcal{T}_w(a_p) \rangle = \langle \mathcal{T}_w(a'_p) \rangle$, that leads to a confusion on size separation of sABPs. To address the issue, we have introduced an additional index that can uniquely identify the size of each sABP. As seen in the inset of panel (a) of Fig. 4, the mean of wall spreading along the y-axis, represented by $\langle \mathcal{Y}_w \rangle$, indicates that there is no overlap in wall accumulation between the size range in the white and yellow areas.

Therefore, we can differentiate samples of micro-agents of varying sizes by utilizing a composite index that integrates both the mean of wall arrival times, $\langle \mathcal{T}_w(a_p) \rangle$, and the mean of wall spreading along the y-axis, $\langle \mathcal{Y}_w \rangle$. Moreover, as illustrated in panel (a) of Fig. 4, the increasing error bars associated with wall arrival times for sizes diverging from the unit size ($a_p = 1$) emphasize the growing uncertainty in the sorting accuracy for larger or smaller micro-agents. This observation necessitated the introduction of a new metric to estimate the error in the sorting mechanism of micro-agents with distinct sizes.

To quantify this potential sorting error, we analyze the co-occurrence of wall arrival times for sABPs of different sizes by examining how often events fall into the same histogram bins, as shown in panel (b) of Fig. 4. When two particles reach the wall simultaneously, their arrival times are recorded within the same time interval. By evaluating these co-occurrence events, we can assess the separability error and, consequently, the effectiveness of the size-sorting mechanism.

When the wall arrival time distributions of sABPs with different sizes become more similar, there is an increase in the number of shared events in the histogram bins. This effect is illustrated in panel (b) of Fig. 4, which displays the wall arrival time histograms for two sets of simulations with different particle sizes ($a_p = 2$ and $a_p = 3$). As the histogram overlap increases, so does the likelihood of misclassification and errors in sorting particles.

The Relative Separability Measure (RSM) provides a quantitative way to assess the degree of overlap between the wall arrival time distributions of sABPs with different sizes. The equation for RSM is given as:

$$\text{RSM}(a_p, a'_p) = \sum_{i=1}^n \min\{\mathcal{T}_w(a_p)_i, \mathcal{T}_w(a'_p)_i\}, \quad (8)$$

where a_p and a'_p represent two different particle sizes, $\mathcal{T}_w(a_p)_i$ and $\mathcal{T}_w(a'_p)_i$ represent the counts of particles with sizes a_p and a'_p that arrive at the wall during time interval i , and n is the total number of histogram bins representing different time intervals. The RSM function is obtained by summing up the minimum counts across all bins.

Panel (c) of Fig. 4 shows a 2D histogram of the RSM function. As the RSM function approaches zero, the graph turns blue, and as it approaches one, it turns red. The histogram highlights areas where the sorting mechanism may face difficulty in the separation of different sizes (pairs of sizes a_p and a'_p). The more the histogram tends towards red, the harder it becomes to separate distinct sizes. On the other hand, blue-tailed data points make distinguishability easier.

B. Size-based particle sorting mechanism in the presence of thermal noises

So far, we have eliminated the thermal noises during the simulation with the A2C method. Moving forward, we plan to expand simulations to include cases where the simulation Péclet number equals a finite value $\text{Pe}^{\text{sim}} \neq \infty$, and analyze the scenarios depicted in the three lower panels of Fig. 4. In this part, we will introduce added thermal noise to the simulations to analyze the results further.

In Fig. 4, panels (d), (e), and (f) display simulations of sABPs, exposed to thermal noises characterized by $\text{Pe}^{\text{sim}} = 10^2$ within the range of \mathcal{A}_p . As the size of sABP shifts away from the predetermined value of training $a_p = 1$, the error bars steadily grow, as shown in panel (d). This behavior is also observed in simulations conducted with $\text{Pe}^{\text{sim}} = \infty$ (in the absence of thermal noises. see upper panels of Fig. 4), as previously discussed in Sec. IV A. The key difference is that the noisy background contributes to a greater increase in error bars in wall arrival times across nearly all sizes of the agents. To provide a more visualized example, we show that the wall arrival time distribution widens for two specific sizes of a_p , namely $a_p = 2$ and $a_p = 3$, as shown in panel (e) compared to panel (b). We also present the RSM function (as defined earlier in Eq. 8) in panel (f) to demonstrate how the blue-tailed regions are affected accordingly. In panel (f), the blue-tailed areas appear to get shrunk compared to panel (c). However, this observation is merely a qualitative analysis; we'll introduce a new measure called the Effective Separability Measure (ESM) later to quantify how these shrunk areas can be influenced. This new quantity allows us to estimate how effectively the size-based particle sorting mechanism can

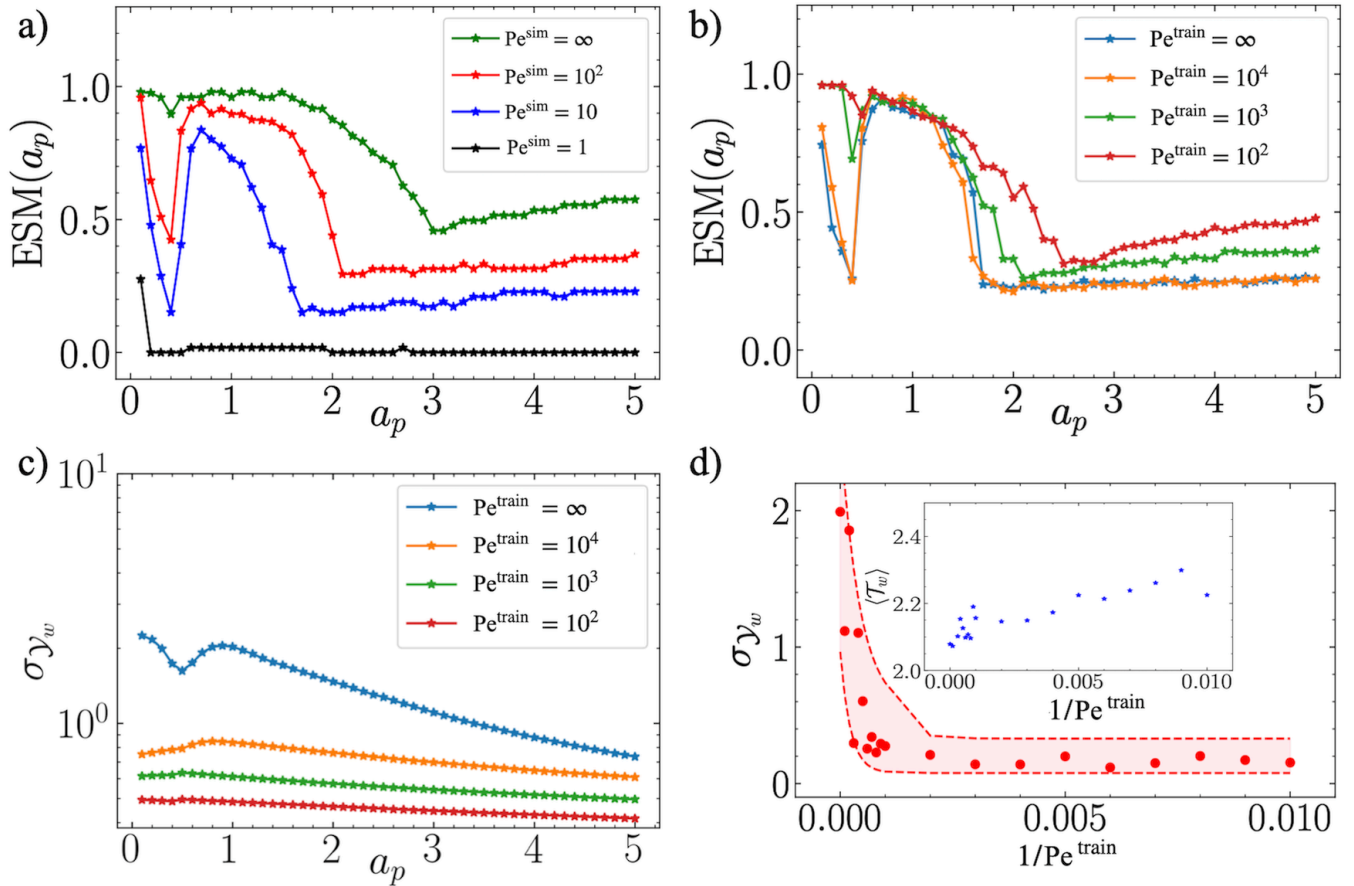


Figure 5. Panel (a): ESM in exposing to different intensity levels of $Pe^{\text{sim}} = \{\infty, 10^2, 10, 1\}$. Panel (b): ESM values in a selected range of sizes $\mathcal{A}_p = \{0.1, \dots, 5.0\}$, trained with different levels of $Pe^{\text{train}} = \{\infty, 10^4, 10^3, 10^2\}$ and in exposing to the fixed value of thermal noises with $Pe^{\text{sim}} = 10^2$. Panel (c): The standard deviation of vertical spreading of sABPs in the range of sizes \mathcal{A}_p . These measurements are conducted through the simulations after the particles had been trained with different values of $Pe^{\text{train}} = \{\infty, 10^4, 10^3, 10^2\}$. Panel (d): Standard deviation of unit size sABPs. In the inset, the mean wall arrival time $\langle \mathcal{T}_w \rangle$ of agents are demonstrated over different values of $1/Pe^{\text{train}}$.

distinguish a sABP of a specific size from all other sABPs of different sizes. Based on this quantity, we can assign a value to the efficiency of the size-based particle sorting mechanism as follows:

$$ESM(a_p) = \frac{\sum_{a_p \neq a'_p} [1 - RSM(a_p, a'_p)] (RSM(a_p, a'_p) > R_t)}{N - 1}. \quad (9)$$

In this equation, $N - 1$ is the number of distinct sizes of our sorting mechanism that $a'_p \neq a_p$. Calculating the ESM value of a specific size a_p involves using a formula that adds up $(1 - RSM)$ values as a successful separation index defined between the size a_p and all other sizes a'_p . Here, if the RSM value exceeds a certain threshold R_t , the term will be included in the summation. We can

alter the criteria for differentiating between two sizes by adjusting the threshold value, denoted as R_t .

Finally, in panel (a) of Fig. 5, we present the ESM values (by setting the threshold value $R_t = 0.1$) obtained from 2D histograms of RSM function for different values of $Pe^{\text{sim}} = \{\infty, 10^4, 10^2, 1\}$ in regarding to different sizes. Examining panel (a) of Fig. 5, it becomes apparent that by decreasing Pe^{sim} , the ESM value shifts significantly towards lower values for almost every sizes analyzed. Therefore, as the noise level gradually increases, it becomes more difficult to distinguish between different sizes in the simulation workspace.

C. Effect of noise-induced training with $Pe^{\text{train}} \neq \infty$ on the size-based particle sorting mechanism

In Sec. IV B, we previously analyzed the noise-free case of training agents in a noisy background. Now, we turn our attention to how the size-based particle sorting mechanism behaves when agents are trained with different values of $Pe^{\text{train}} \neq \infty$ and are later exposed to thermal noise with a fixed intensity level, Pe^{sim} in the simulation stage. In this part, we train the sABPs under the condition $Pe^{\text{train}} \geq Pe^{\text{sim}}$. Hereafter, we will use 'train' and 'sim' to refer to the thermal noise conditions during the training and simulation stages, respectively.

Panel (b) of Fig. 5 shows how noise-induced training affects the simulation when sABPs are exposed to thermal noise with $Pe^{\text{sim}} = 10^2$ during the simulation stage. After analyzing the results of noise-induced training with different values of $Pe^{\text{train}} = \{\infty, 10^4, 10^3, 10^2\}$, we observe that as the train Péclet number decreases, the efficiency of size separation (represented by the ESM values) improves for nearly all micro-agent sizes, as illustrated in panel (b) of Fig. 5.

Furthermore, decreasing the train Péclet number towards the simulation Péclet number, $Pe^{\text{train}} \rightarrow Pe^{\text{sim}}$, results in a significant reduction in the standard deviation of vertical spreading, σ_{y_w} , for micro-agents reaching the wall area during the simulation. Panel (c) of Fig. 5 displays the simulation results for micro-agents of sizes belonging to \mathcal{A}_p , under the four different train Péclet numbers. These results indicate a more concentrated accumulation around the target domain along the wall area when exposed to thermal noise with $Pe^{\text{sim}} = 10^2$.

Finally, panel (d) of Fig. 5 provides insight into the impact on the specific agent size $a_p = 1$, particularly regarding the standard deviation σ_{y_w} . Despite a gradual increase in the mean wall arrival time $\langle \mathcal{T}_w \rangle$, as shown in the inset of panel (d), the standard deviation of the vertical spreading σ_{y_w} decays completely as the inverse train Péclet number increases from $1/Pe^{\text{train}} = 0$ to $1/Pe^{\text{train}} = 10^{-2}$. It shows that although the micro-agents take a longer time to reach the wall area, on average, they gather at a more concentrated region on the wall area. This effect represents a new discovery that emerged from our noise-induced training method, which was not intuitively anticipated.

V. CONCLUDING REMARKS

In this study, we have surveyed the application of DRL, specifically using the A2C method, for the optimal navigation of the sABP in a dynamic environment with a rotating Gaussian potential. We also have studied the sABP in the scenarios where the training stage Péclet number $Pe^{\text{train}} \geq 10^2$ and the simulation (testing) stage Péclet number $Pe^{\text{sim}} \geq 1$. The results show that the A2C method effectively enables sABPs to navigate through

complex, time-varying landscapes and reach target destinations in the shortest possible time.

We have validated the approach through extensive simulations, confirming the robustness and efficiency of the learned navigation strategies. Additionally, we have explored the implications of our method for size-based separation of sABPs. By leveraging the mean wall arrival times besides the mean vertical wall spreading (as a mixed metric) and additionally introducing a novel measure RSM, we successfully identified and separated sABPs based on their sizes. Our analysis revealed that the size-based particle sorting mechanism remains effective even in the presence of thermal noises, with the ESM providing a quantitative assessment of the size-based sorting accuracy.

Furthermore, we investigated the impact of noise-induced training on our size-based particle sorting mechanism. Training sABPs in noisy environments revealed an improvement compared to noise-free trained cases in the resilience and accuracy of size-based particle sorting during simulations with thermal noises. This approach highlights the potential of noise-induced training in enhancing the robustness of DRL-based navigation strategies under realistic conditions.

Our findings suggest promising avenues for future research, including the application of DRL techniques to other complex navigation and control problems in micro-scale environments. The ability to dynamically adapt and optimize navigation strategies in the presence of uncertainties holds significant potential for advancements in autonomous systems and active matter research.

CONFLICTS OF INTEREST

There are no conflicts of interest to declare.

AUTHOR CONTRIBUTIONS

Mohammad Hossein Masoudi: Data curation; formal analysis (lead); investigation (lead); methodology; software; validation (lead); visualization; writing – original draft preparation (lead); writing – review and editing (equal). **Ali Naji:** Conceptualization; formal analysis (supporting); project administration; funding acquisition; investigation (supporting); supervision; validation (supporting); writing – original draft preparation (supporting); writing – review and editing (equal).

ACKNOWLEDGMENT

A.N. would like to acknowledge support from the ICTP (Trieste, Italy) through the Associates Programme and from the Simons Foundation through grant number 284558FY19. MHM acknowledges the support provided

through the same grant for a visit to the ICTP during this research.

DATA AVAILABILITY STATEMENT

The data supporting the results of this study are available within the article.

-
- [1] M. C. Marchetti, J. F. Joanny, S. Ramaswamy, T. B. Liverpool, J. Prost, M. Rao, and R. A. Simha, *Hydrodynamics of soft active matter*, *Rev. Mod. Phys.* **85**, 1143 (2013).
- [2] J. Elgeti, R. G. Winkler, and G. Gompper, *Physics of microswimmer–single particle motion and collective behavior: a review*, *Rep. Prog. Phys.* **78**, 056601 (2015).
- [3] C. Bechinger, R. Di Leonardo, H. Löwen, C. Reichhardt, G. Volpe, and G. Volpe, *Active particles in complex and crowded environments*, *Rev. Mod. Phys.* **88**, 045006 (2016).
- [4] W. F. Paxton, K. C. Kistler, C. C. Olmeda, A. Sen, S. K. St. Angelo, Y. Cao, T. E. Mallouk, P. E. Lammert, and V. H. Crespi, *Catalytic nanomotors: Autonomous movement of striped nanorods*, *J. Am. Chem. Soc.* **126**, 13424 (2004).
- [5] T. Vicsek and A. Zafeiris, *Collective motion*, *Phys. Rep.* **517** (2010).
- [6] M. Cates and J. Tailleur, *Motility-induced phase separation*, *Annu. Rev. Condens. Matter Phys.* **6** (2014).
- [7] A. P. Solon and et al., *Pressure is not a state function for generic active fluids*, *Nature Physics* **11**, 673 (2015).
- [8] H. Chaté, F. Ginelli, G. Grégoire, and F. Raynaud, *Collective motion of self-propelled particles interacting without cohesion*, *Phys. Rev. E* **77**, 046113 (2008).
- [9] F. Ginelli, F. Peruani, M. Bär, and H. Chaté, *Large-scale collective properties of self-propelled rods*, *Phys. Rev. Lett.* **104**, 184502 (2010).
- [10] A. Zöttl and H. Stark, *Emergent behavior in active colloids*, *J. Condens. Matter Phys.* **28**, 253001 (2016).
- [11] E. Lauga, *Bacterial hydrodynamics*, *Annu. Rev. Fluid Mech.* **48**, 105 (2016).
- [12] J. Toner, Y. Tu, and S. Ramaswamy, *Hydrodynamics and phases of flocks*, *Ann Phys (N Y)* **318**, 170 (2005).
- [13] I. Buttinoni, J. Bialké, F. Kümmel, H. Löwen, C. Bechinger, and T. Speck, *Dynamical clustering and phase separation in suspensions of self-propelled colloidal particles*, *Phys. Rev. Lett.* **110**, 238301 (2013).
- [14] A. Zöttl and H. Stark, *Nonlinear dynamics of a microswimmer in poiseuille flow*, *Phys. Rev. Lett.* **108**, 218104 (2012).
- [15] K. Son, D. R. Brumley, and R. Stocker, *Live from under the lens: exploring microbial motility with dynamic imaging and microfluidics*, *Nat. Rev. Microbiol.* **13**, 761 (2015).
- [16] J. Yan, M. Bloom, S. C. Bae, E. Luijten, and S. Granick, *Reconfiguring active particles by electrostatic imbalance*, *Nat. Mater* **15**, 1095 (2016).
- [17] G. S. Redner, M. F. Hagan, and A. Baskaran, *Structure and dynamics of a phase-separating active colloidal fluid*, *Phys. Rev. Lett.* **110**, 055701 (2013).
- [18] I. Theurkauff, C. Cottin-Bizonne, J. Palacci, C. Ybert, and L. Bocquet, *Dynamic clustering in active colloidal suspensions with chemical signaling*, *Phys. Rev. Lett.* **108**, 268303 (2012).
- [19] P. Romanczuk, M. Bär, W. Ebeling, B. Lindner, and L. Schimansky-Geier, *Active brownian particles. from individual to collective stochastic dynamics*, *Eur Phys J Spec Top.* **202**, 1 (2012).
- [20] I. Gibbons, *Cilia and flagella of eukaryotes*, *J. Cell Biol.* **91**, 107s (1982).
- [21] H. C. Berg, *The rotary motor of bacterial flagella*, *Annu. Rev. Biochem.* **72**, 19 (2003).
- [22] J. R. Howse, R. A. L. Jones, A. J. Ryan, T. Gough, R. Vafabakhsh, and R. Golestanian, *Self-motile colloidal particles: From directed propulsion to random walk*, *Phys. Rev. Lett.* **99**, 048102 (2007).
- [23] D. V. Rao, N. Reddy, J. Franssaer, and C. Clasen, *Self-propulsion of bent bimetallic janus rods*, *J. Phys. D: Appl. Phys.* **52**, 014002 (2018).
- [24] E. Poggi and J.-F. Gohy, *Janus particles: from synthesis to application*, *Colloid Polym. Sci.* **295**, 2083 (2017).
- [25] M. Bär, R. Großmann, S. Heidenreich, and F. Peruani, *Self-propelled rods: Insights and perspectives for active matter*, *Annu. Rev. Condens. Matter Phys.* **11**, 441 (2020).
- [26] H. C. Berg and E. M. Purcell, *Physics of chemoreception*, *Biophysical journal* **20**, 193 (1977).
- [27] J. Palacci, S. Sacanna, A. P. Steinberg, D. J. Pine, and P. M. Chaikin, *Living crystals of light-activated colloidal surfers*, *Science* **339**, 936 (2013).
- [28] R. E. Goldstein, *Green algae as model organisms for biological fluid dynamics*, *Annu. Rev. Fluid Mech.* **47**, 343 (2015).
- [29] R. P. Blakemore, *Magnetotactic bacteria*, *Science (New York, N.Y.)* **190**, 377 (1975).
- [30] K. Erglis, Q. Wen, V. Ose, A. Zeltins, A. Sharipo, P. Janmey, and A. Cebers, *Dynamics of magnetotactic bacteria in a rotating magnetic field*, *Biophysical journal* **93**, 1402 (2007).
- [31] M. R. Shabanniya and A. Naji, *Active dipolar spheroids in shear flow and transverse field: Population splitting, cross-stream migration, and orientational pinning*, *J. Chem. Phys.* **152** (2020).
- [32] M. C. Marchetti, Y. Fily, S. Henkes, A. Patch, and D. Yllanes, *Minimal model of active colloids highlights the role of mechanical interactions in controlling the emergent behavior of active matter*, *Current Opinion in Colloid & Interface Science* **21**, 34 (2016).

- [33] E. Schneider and H. Stark, Optimal steering of a smart active particle, *EPL* **127**, 64003 (2019).
- [34] S. Colabrese, K. Gustavsson, A. Celani, and L. Biferale, Flow navigation by smart microswimmers via reinforcement learning, *Phys. Rev. Lett.* **118**, 158004 (2017).
- [35] K. Gustavsson, L. Biferale, A. Celani, and S. Colabrese, Finding efficient swimming strategies in a three-dimensional chaotic flow by reinforcement learning, *Eur Phys J E Soft Matter EUR PHYS J E* **40**, 110 (2017).
- [36] L. Biferale, F. Bonaccorso, M. Bucciotti, P. Clark Di Leoni, and K. Gustavsson, Zermelo’s problem: optimal point-to-point navigation in 2d turbulent flows using reinforcement learning, *Chaos* **29** (2019).
- [37] M. Nasiri and B. Liebchen, Reinforcement learning of optimal active particle navigation, *New J. Phys.* **24**, 073042 (2022).
- [38] P. Gunnarson, I. Mandralis, G. Novati, P. Koumoutsakos, and J. O. Dabiri, Learning efficient navigation in vortical flow fields, *Nat. Comm.* **12**, 7143 (2021).
- [39] M. Bucciotti, L. Biferale, F. Bonaccorso, P. Clark di Leoni, and K. Gustavsson, Optimal control of point-to-point navigation in turbulent time dependent flows using reinforcement learning (2021) pp. 223–234.
- [40] Z. Zou, Y. Liu, Y. N. Young, O. S. Pak, and A. C. H. Tsang, Gait switching and targeted navigation of microswimmers via deep reinforcement learning, *Commun. Phys.* **5**, 158 (2022).
- [41] F. Borra, L. Biferale, M. Cencini, and A. Celani, Reinforcement learning for pursuit and evasion of microswimmers at low reynolds number, *Phys. Rev. Fluids* **7**, 023103 (2022).
- [42] S. Muiños-Landin, A. Fischer, V. Holubec, and F. Cichos, Reinforcement learning with artificial microswimmers, *Sci. Robot.* **6**, eabd9285 (2021).
- [43] M. Putzke and H. Stark, Optimal navigation of a smart active particle: directional and distance sensing, *The European Physical Journal E* **46**, 48 (2023).
- [44] C. Calascibetta, L. Biferale, F. Borra, A. Celani, and M. Cencini, Optimal tracking strategies in a turbulent flow, *Communications Physics* **6**, 256 (2023).
- [45] P. Gunnarson, I. Mandralis, G. Novati, P. Koumoutsakos, and J. O. Dabiri, Learning efficient navigation in vortical flow fields, *Nat. Comm.* **12**, 7143 (2021).
- [46] K. Son, D. R. Brumley, and R. Stocker, Live from under the lens: exploring microbial motility with dynamic imaging and microfluidics, *Nature Reviews Microbiology* **13**, 761 (2015).
- [47] C. W. Shields, C. D. Reyes, and G. P. López, Microfluidic cell sorting: a review of the advances in the separation of cells from debulking to rare cell isolation, *Lab Chip* **15**, 1230 (2015).
- [48] A. Lenshof and T. Laurell, Continuous separation of cells and particles in microfluidic systems, *Chemical Society Reviews* **39**, 1203 (2010).
- [49] R. S. Sutton and A. G. Barto, *Reinforcement Learning: An Introduction* (MIT press Cambridge, 2018).
- [50] C. Zhou, B. Huang, and P. Fränti, A review of motion planning algorithms for intelligent robots, *J. Intell. Manuf.* **33**, 387 (2022).
- [51] M. Morales, *Grokking Deep Reinforcement Learning* (Manning Publications, 2020).
- [52] A. Paszke, S. Gross, F. Massa, A. Lerer, J. Bradbury, G. Chanan, T. Killeen, Z. Lin, N. Gimelshein, L. Antiga, *et al.*, Pytorch: An imperative style, high-performance deep learning library, *Advances in Neural Information Processing Systems* **32**, 8024 (2019).
- [53] D. Kularatne, S. Bhattacharya, and M. A. Hsieh, Going with the flow: a graph based approach to optimal path planning in general flows, *Autonomous Robots* **42**, 1369 (2018).